Estimation and diagnosis of heterogeneous flow-dependent background-error covariances at the convective scale using either large or small ensembles

Benjamin Ménétrier,* Thibaut Montmerle, Loïk Berre and Yann Michel

Centre National de Recherches Météorologiques (CNRM), Toulouse, France

*Correspondence to: B. Ménétrier, Météo-France/CNRM/GAME, 42 av. G. Coriolis, 31057 Toulouse, France.
E-mail: benjamin.menetrier@meteo.fr

A 90 member ensemble assimilation experiment is run on a severe weather event for the convective-scale Application de la Recherche à l'Opérationnel à Méso-Echelle (model AROME-France), coupled to a global 90 member Action de Recherche Petite Echelle Grande Echelle (ARPEGE) ensemble. Background-error covariances are diagnosed for this period, in order to examine flow-dependent features, sampling noise effects associated with six-member estimates (corresponding to the size of a preliminary research AROME ensemble) and a comparison between AROME and ARPEGE estimates. The dependence of error covariances on the weather situation is illustrated for low-level specific humidity in particular, which is associated, for example, with large variance values over the Mediterranean area. While this large-scale contrast is visible in both AROME and ARPEGE ensembles, differences between the two ensembles are also apparent as expected, for instance due to resolution differences. The effects of sampling noise are investigated by comparing independent six-member and 84 member estimates of variances and correlation length-scales. While the six-member ensemble is able to capture some of the signal of interest, spatial filtering techniques seem to be useful in order to reduce estimation errors.

Key Words: background-error variances; background-error local correlation Hessian tensor; convective scale; ensemble assimilation.

Received 13 June 2013; Revised 30 September 2013; Accepted 5 October 2013; Published online in Wiley Online Library 9 January 2014

1. Introduction

Numerical weather prediction (NWP) models are very chaotic systems, so that the initial state error grows fast as the forecast range stretches (Lorenz, 1963). As a consequence, the initial state estimation has to be carried out very carefully. This is the role of data assimilation, which aims to combine information from several sources in an optimal way in order to define an initial state called 'analysis'. Although numerous algorithms are available for such a task, only a few can be run operationally at an affordable computational cost, given the huge size of operational NWP model states ($\sim 10^8$ elements) and the increasing number of observations that are assimilated ($\sim 10^5$ for Application of Research to Operations at Mesoscale (AROME-France)). Ensemble-based algorithms such as the ensemble Kalman filter (EnKF: Evensen, 1994) or the ensemble variational algorithm (En-Var: Liu *et al.*, 2008, 2009; Buehner *et al.*, 2009a,b) might be performed at a reasonable computational cost for global models, since lower resolution runs can compensate for the cost of ensemble forecasts. However, this strategy seems to be difficult to afford for convective-scale models, for the time being, especially because of the high central processing unit (CPU) cost required

by the non-hydrostatic dynamics and the explicit resolution of cloud processes.

At Météo-France, the convective-scale model AROME (Seity *et al.*, 2011) has been operational since the end of 2008 and its lateral boundary conditions are provided by the global ARPEGE system. The AROME-France model analysis comes from from a three-dimensional variational (3D-Var) scheme (Le Dimet and Talagrand, 1986). In such a system, background-error covariances have a deep impact on the analysis, since they are used to filter and propagate information provided by observations (Daley, 1991). Moreover, because of its prohibitive size ($\sim (10^8)^2$ elements), this covariance matrix needs to be modelled in the form of a sequence of sparse operators. In the current operational configuration, a time-averaged spectral covariance model is used, leading to specified covariance functions that are static, homogeneous and isotropic (Berre, 2000).

The currently specified static covariances are estimated using an AROME ensemble data assimilation approach (Brousseau *et al.*, 2011). This is based on an ensemble of perturbed and cycled data assimilation experiments, the aim of which is to simulate the error evolution during the AROME data assimilation cycling. While this AROME ensemble is currently run offline to derive static,

homogeneous and isotropic covariances, it is planned in future to run such a high-resolution ensemble in real time. This would provide flow-dependent covariance estimates and also initial perturbations for high-resolution ensemble predictions. This is supported by recent studies (Caron and Fillion, 2010; Michel and Auligné, 2010; Monteiro and Berre, 2010; Montmerle and Berre, 2010; Brousseau *et al.*, 2011, 2012), which indicate that actual covariances should be rather heterogeneous and flow-dependent. This means that our current system assimilates observations in a sub-optimal way, especially during intense weather events, where overconfidence is likely to be given to an uncertain background state.

In order to use perturbed lateral boundary conditions, the AROME ensemble (hereafter called Assimilation d'Ensemble AROME (AEARO)) can be coupled with the global AEARP ensemble, which is based on the ARPEGE model. This global ensemble data assimilation system has been operational at Météo-France since July 2008 (Berre and Desroziers, 2010). It is currently based on six perturbed members and 4D-Var, in order to simulate the error evolution of the deterministic ARPEGE 4D-Var system. The Assimilation d'Ensemble ARPEGE (AEARP) ensemble provides flow-dependent variances to the ARPEGE 4D-Var system and also initial perturbations to Prévision d'Ensemble ARPEGE (PEARP), which is the global ensemble prediction system based on ARPEGE at Météo-France (Descamps and Labadie, 2009).

The current article is based on a case study for diagnosing features corresponding to flow-dependent error covariances that are provided by the experimental AROME ensemble. One aim is to examine connections between error covariances and intense weather events, such as those taking place over the Western Mediterranean area in the frame of the Hydrological cycle in the Mediterranean EXperiment (HYMEX).[†] In order to document these connections using robust covariance estimates, large ensembles have been run, based on 90 members. Moreover, since a six-member AROME ensemble is planned as a research experiment, a second aim of the article is to examine sampling noise effects for such a six-member ensemble and their possible treatment using filtering techniques (e.g. Raynaud *et al.*, 2009; Berre and Desroziers, 2010). Finally, a comparison between AROME and ARPEGE error estimates has been carried out, in order to document AROME features that are either common with ARPEGE or specific to AROME, due for instance to resolution and data assimilation differences.

In section 2, the error simulation method and the covariance estimation are formally presented, with an insight regarding the diagnostics, which correspond to background-error variances, local correlation Hessian tensors (hereafter denoted as LCH tensors) and length-scales. The experimental set-up is described in section 3. The results are detailed and discussed in section 4 for variances and in section 5 for correlation diagnostics.

2. Simulation of errors and covariance estimation

An ensemble of perturbed forecasts can be used to estimate forecast-error covariances, but this estimation is affected by several sources of error. In this section, the link between error covariances and perturbation covariances is detailed, as well as the nature of covariance estimation errors.

2.1. Analysis and forecast-error dynamics

The analysis state $\mathbf{x}^a$ and the background state $\mathbf{x}^b$ of e.g. a 3D-Var deterministic system are cycled in two steps, according to the

---

[†]www.hymex.org

analysis and forecast equations:

$$\begin{cases} \mathbf{x}^a = \mathbf{x}^b + \overline{\mathbf{K}}(\mathbf{y}^o - \overline{H}(\mathbf{x}^b)), \\ \mathbf{x}^{b+} = M(\mathbf{x}^a), \end{cases} \quad (1)$$

where $\overline{\mathbf{K}} = \overline{\mathbf{B}}\,\overline{\mathbf{H}}^T(\overline{\mathbf{H}}\overline{\mathbf{B}}\,\overline{\mathbf{H}}^T + \overline{\mathbf{R}})^{-1}$ is the specified gain matrix. $\overline{H}$ and $\overline{\mathbf{H}}$ correspond respectively to the nonlinear observation operator and to its linearized version. $\overline{\mathbf{B}}$ and $\overline{\mathbf{R}}$ are the specified background- and observation-error covariance matrices. M is the forecast model and the $+$ superscript indicates vectors of the next analysis cycle. At first order, the analysis and forecast errors dynamics are given by

$$\begin{cases} \boldsymbol{\varepsilon}^a = (\mathbf{I} - \overline{\mathbf{K}}\overline{\mathbf{H}})\boldsymbol{\varepsilon}^b + \overline{\mathbf{K}}\boldsymbol{\varepsilon}^o, \\ \boldsymbol{\varepsilon}^{b+} = \mathbf{M}\boldsymbol{\varepsilon}^a + \boldsymbol{\varepsilon}^m, \end{cases} \quad (2)$$

where $\mathbf{M}$ is the tangent-linear forecast model, $\boldsymbol{\varepsilon}^o$ is the observation error and $\boldsymbol{\varepsilon}^m$ is the model error. Assuming that errors are unbiased, that background and observation errors are uncorrelated (namely $\mathbb{E}[\mathbf{H}\boldsymbol{\varepsilon}^b(\boldsymbol{\varepsilon}^o)^T] = 0$, where $\mathbb{E}[\,\cdot\,]$ is the expectation operator) and that analysis and model errors are uncorrelated (i.e. $\mathbb{E}[\mathbf{M}\boldsymbol{\varepsilon}^a(\boldsymbol{\varepsilon}^m)^T] = 0$), analysis and forecast-error covariances are cycled by

$$\begin{cases} \mathbf{A} = (\mathbf{I} - \overline{\mathbf{K}}\overline{\mathbf{H}})\mathbf{B}(\mathbf{I} - \overline{\mathbf{K}}\overline{\mathbf{H}})^T + \overline{\mathbf{K}}\mathbf{R}\overline{\mathbf{K}}^T, \\ \mathbf{B}^+ = \mathbf{M}\mathbf{A}\mathbf{M}^T + \mathbf{Q}, \end{cases} \quad (3)$$

where $\mathbf{R} = \mathbb{E}[\boldsymbol{\varepsilon}^o(\boldsymbol{\varepsilon}^o)^T]$ and $\mathbf{Q} = \mathbb{E}[\boldsymbol{\varepsilon}^m(\boldsymbol{\varepsilon}^m)^T]$.

2.2. Ensemble perturbation dynamics

To simulate analysis and forecast-error evolution during the data assimilation cycling, a common strategy is to use an ensemble of perturbed analysis and forecasts. This method, hereafter called ensemble data assimilation (EDA), aims to approximate the true error covariances with ensemble perturbation covariances.

In particular, we will consider the case where explicit observation perturbations $\boldsymbol{\delta}^o$ and model perturbations $\boldsymbol{\delta}^m$ are added to simulate observation errors and model errors respectively. In practice, these perturbations can be obtained as random draws of specified error covariances $\overline{\mathbf{R}}$ and $\overline{\mathbf{Q}}$. Due to the data assimilation cycling, analysis and background are implicitly perturbed by $\boldsymbol{\delta}^a$ and $\boldsymbol{\delta}^b$ respectively. At first order, the analysis and forecast perturbations dynamics is given by

$$\begin{cases} \boldsymbol{\delta}^a = (\mathbf{I} - \overline{\mathbf{K}}\overline{\mathbf{H}})\boldsymbol{\delta}^b + \overline{\mathbf{K}}\boldsymbol{\delta}^o, \\ \boldsymbol{\delta}^{b+} = \mathbf{M}\boldsymbol{\delta}^a + \boldsymbol{\delta}^m. \end{cases} \quad (4)$$

To compute covariances from an ensemble of N perturbations, we use an estimator Cov_N that has bilinearity properties, $\mathbf{F}$ being any linear operator and $\boldsymbol{\delta}$, $\boldsymbol{\delta}'$ and $\boldsymbol{\delta}''$ being any perturbation:

$$\text{Cov}_N(\mathbf{F}\boldsymbol{\delta} + \boldsymbol{\delta}', \boldsymbol{\delta}'') = \mathbf{F}\,\text{Cov}_N(\boldsymbol{\delta}, \boldsymbol{\delta}'') + \text{Cov}_N(\boldsymbol{\delta}', \boldsymbol{\delta}''),$$

$$\text{Cov}_N(\boldsymbol{\delta}, \mathbf{F}\boldsymbol{\delta}' + \boldsymbol{\delta}'') = \text{Cov}_N(\boldsymbol{\delta}, \boldsymbol{\delta}')\mathbf{F}^T + \text{Cov}_N(\boldsymbol{\delta}, \boldsymbol{\delta}'').$$

Estimated analysis and background perturbation covariances are thus given by

$$\begin{cases} \widetilde{\mathbf{A}} = \text{Cov}_N(\boldsymbol{\delta}^a, \boldsymbol{\delta}^a) \\ \quad = (\mathbf{I} - \overline{\mathbf{K}}\overline{\mathbf{H}})\widetilde{\mathbf{B}}(\mathbf{I} - \overline{\mathbf{K}}\overline{\mathbf{H}})^T + \overline{\mathbf{K}}\widetilde{\mathbf{R}}\overline{\mathbf{K}}^T \\ \quad\quad + (\mathbf{I} - \overline{\mathbf{K}}\overline{\mathbf{H}})\,\text{Cov}_N(\boldsymbol{\delta}^b, \boldsymbol{\delta}^o)\overline{\mathbf{K}}^T \\ \quad\quad + \overline{\mathbf{K}}\,\text{Cov}_N(\boldsymbol{\delta}^o, \boldsymbol{\delta}^b)(\mathbf{I} - \overline{\mathbf{K}}\overline{\mathbf{H}})^T, \\ \widetilde{\mathbf{B}}^+ = \text{Cov}_N(\boldsymbol{\delta}^{b+}, \boldsymbol{\delta}^{b+}) \\ \quad = \mathbf{M}\widetilde{\mathbf{A}}\mathbf{M}^T + \widetilde{\mathbf{Q}} \\ \quad\quad + \mathbf{M}\,\text{Cov}_N(\boldsymbol{\delta}^a, \boldsymbol{\delta}^m) \\ \quad\quad + \text{Cov}_N(\boldsymbol{\delta}^m, \boldsymbol{\delta}^a)\mathbf{M}^T, \end{cases} \quad (5)$$

where $\widetilde{\mathbf{R}} = \mathrm{Cov}_N(\boldsymbol{\delta}^\mathrm{o}, \boldsymbol{\delta}^\mathrm{o})$ and $\widetilde{\mathbf{Q}} = \mathrm{Cov}_N(\boldsymbol{\delta}^\mathrm{m}, \boldsymbol{\delta}^\mathrm{m})$.

In the asymptotic limit of infinite ensemble size, cross-covariances such as $\mathrm{Cov}_N(\boldsymbol{\delta}^\mathrm{b}, \boldsymbol{\delta}^\mathrm{o})$ vanish, whereas estimated autocovariances of explicit perturbations (i.e. $\boldsymbol{\delta}^\mathrm{o}$ and $\boldsymbol{\delta}^\mathrm{m}$) converge toward the specified covariances (i.e. $\overline{\mathbf{R}}$ and $\overline{\mathbf{Q}}$). This leads to

$$\begin{cases} \widetilde{\mathbf{A}}^* = \lim_{N\to\infty} \widetilde{\mathbf{A}} \\ \quad = (\mathbf{I} - \overline{\mathbf{K}}\overline{\mathbf{H}})\widetilde{\mathbf{B}}^*(\mathbf{I} - \overline{\mathbf{K}}\overline{\mathbf{H}})^\mathrm{T} + \overline{\mathbf{K}}\overline{\mathbf{R}}\overline{\mathbf{K}}^\mathrm{T}, \\ \widetilde{\mathbf{B}}^{*+} = \lim_{N\to\infty} \widetilde{\mathbf{B}}^+ \\ \quad = \mathbf{M}\widetilde{\mathbf{A}}^*\mathbf{M}^\mathrm{T} + \overline{\mathbf{Q}}. \end{cases} \quad (6)$$

2.3. Covariance estimation errors

In the case where the EDA system shares the same configuration as the deterministic model (resolution, data assimilation, . . .), using the finite-size estimation of perturbation covariances coming from EDA as a proxy for the true error covariances leads to two kinds of errors:

- systematic errors arising from inaccurate observation-error and model-error covariance specifications, leading to differences between $\widetilde{\mathbf{A}}^*$ and $\mathbf{A}$ as well as between $\widetilde{\mathbf{B}}^*$ and $\mathbf{B}$; and
- random errors arising from subsampling noise, namely $\widetilde{\mathbf{A}} - \widetilde{\mathbf{A}}^*$ and $\widetilde{\mathbf{B}} - \widetilde{\mathbf{B}}^*$.

2.4. Random noise of the sample covariance

We assume that we have an ensemble of perturbations corresponding to a Gaussian distribution of zero mean and $\widetilde{\mathbf{B}}^*$ covariance matrix: $\boldsymbol{\delta}_k \sim \mathcal{N}(0, \widetilde{\mathbf{B}}^*)$, and that our estimator for the covariance matrix is

$$\begin{aligned} \widetilde{\mathbf{B}} &= \mathrm{Cov}_N(\boldsymbol{\delta}, \boldsymbol{\delta}) \\ &= \frac{1}{N-1} \sum_{k=1}^{N} (\boldsymbol{\delta}_k - \langle \boldsymbol{\delta} \rangle)(\boldsymbol{\delta}_k - \langle \boldsymbol{\delta} \rangle)^\mathrm{T}, \end{aligned} \quad (7)$$

where $\langle \boldsymbol{\delta} \rangle$ is the sample mean:

$$\langle \boldsymbol{\delta} \rangle = \frac{1}{N} \sum_{k=1}^{N} \boldsymbol{\delta}_k. \quad (8)$$

In this case, $\widetilde{\mathbf{B}}$ follows a Wishart distribution, which is a generalization to multiple dimensions of the χ^2 distribution, named after the work of Wishart (1928). An updated summary of Wishart's theory can be found in Muirhead (2005). Since the ensemble size available for NWP models is always smaller than the size of the model state, the estimated covariance matrix is always singular (i.e not invertible), as shown by Dykstra (1970). Consequently, there is no explicit probability density function for $\widetilde{\mathbf{B}}$, but we can compute every moment of the distribution using the moment-generating function. In particular, the first moment shows that the estimation is unbiased:

$$\mathbb{E}[\widetilde{\mathbf{B}}] = \mathbb{E}[\widetilde{\mathbf{B}}^*], \quad (9)$$

and the second moment gives the covariances between estimates of two-point covariances for any pairs (i, j) and (k, l):

$$\begin{aligned} \mathbb{E}\left[(\widetilde{B}_{ij} - \mathbb{E}[\widetilde{B}_{ij}])(\widetilde{B}_{kl} - \mathbb{E}[\widetilde{B}_{kl}]) \right] \\ = \frac{1}{N-1}(\widetilde{B}_{ik}^*\widetilde{B}_{jl}^* + \widetilde{B}_{il}^*\widetilde{B}_{jk}^*). \end{aligned} \quad (10)$$

The sampling noise is defined by $\mathbf{B}^\mathrm{e} = \widetilde{\mathbf{B}} - \widetilde{\mathbf{B}}^*$ and its statistical properties are thus given as functions of the true covariance

matrix $\widetilde{\mathbf{B}}^*$ and the ensemble size N. These results can be useful to develop filtering schemes of estimated covariances. For instance, one can use the formula for the covariance of sampling noise on local background-error variances, which can be deduced from Eq. (10) in the case where $i = j$ and $k = l$:

$$\mathbb{E}\left[B_{ii}^\mathrm{e} B_{kk}^\mathrm{e} \right] = \frac{2}{N-1} \widetilde{B}_{ik}^{*2}. \quad (11)$$

This relationship between the noise covariance and the background-error covariance has been employed by e.g. Raynaud *et al.* (2009), in order to reduce sampling noise of estimated variances at the global scale by using an objective Wiener filter (Wiener, 1949).

While the current article will focus on the application of spatial filtering to background-error variances, it may also be mentioned that 'variance filtering' (e.g. Berre and Desroziers, 2010) and 'correlation localization' (e.g. Houtekamer and Mitchell, 2001) are two different approaches, which tend to be complementary, in order to reduce sampling noise effects that affect background-error covariances. This corresponds to the fact that 'localization' is a way to reduce the amount of noise that affects long-distance covariances, while 'variance filtering' allows noise to be reduced at zero separation distances.

2.5. Variances, LCH tensors and length-scales

Without any loss of generality, the estimated background-error covariance matrix can be split into two parts:

$$\widetilde{\mathbf{B}} = \widetilde{\mathbf{V}}^{1/2}\widetilde{\mathbf{C}}\widetilde{\mathbf{V}}^{\mathrm{T}/2}, \quad (12)$$

where $\widetilde{\mathbf{V}}$ is the diagonal matrix of background-error variances and $\widetilde{\mathbf{C}}$ is the background-error correlation matrix.

Background-error variances have the same size as the model state ($\sim 10^8$) and thus can be easily estimated and evaluated as such. Conversely, the background-error correlation matrix size is the square of the model state size ($\sim (10^8)^2$), so that the full correlation matrix cannot be explicitly estimated and evaluated. Therefore, it is convenient to diagnose the curvature at the origin of local correlation functions $c(\mathbf{r})$, where $\mathbf{r}$ is the position vector in a d-dimensional space (with e.g. $d = 2$ in the two-dimensional horizontal case), by using the LCH tensor of second-order derivatives (Weaver and Mirouze, 2012):

$$\boldsymbol{H} = -\nabla\nabla^\mathrm{T}c(\mathbf{r})|_{\mathbf{r}=0}. \quad (13)$$

This tensor is positive-definite, so it can be diagonalized in a basis of orthogonal eigenvectors $\mathbf{e}_\gamma$ with corresponding positive eigenvalues λ_γ. The tensor can be represented by an ellipsoid, the semi-principal axes of which in the $\mathbf{e}_\gamma$ directions are the corresponding length-scales $L_\gamma^\mathrm{b} = \lambda_\gamma^{-1/2}$. The total length-scale L^b can be defined as the geometric average of the semi-principal axes:

$$L^\mathrm{b} = \sqrt[d]{\prod_{\gamma=1}^{d} L_\gamma^\mathrm{b}} = \det(\boldsymbol{H})^{-1/(2d)}. \quad (14)$$

In this study, we shall focus on horizontal correlations only and thus reduce $\boldsymbol{H}$ to a two-dimensional tensor. In this case, the total length-scale L^b is such that the ellipse representing the tensor has the same area as a circle of radius L^b.

3. Experimental framework

3.1. Ensemble data assimilation experiments

In order to simulate AROME forecast errors, a 90 member AROME ensemble experiment has been run, coupled to a

© 2013 Royal Meteorological Society

Q. J. R. Meteorol. Soc. **140**: 2050–2061 (2014)

Table 1. Specific features of ARPEGE and AROME models used in EDA.

	ARPEGE	AROME
Domain	Global	1875 km × 1800 km LAM over France
Horizontal resolution	$T399$ ($\Delta x = 50$ km)	$\Delta x = 2.5$ km
Vertical resolution	$L70$ up to 0.05 hPa	$L60$ up to 1.4 hPa
Dynamics	Hydrostatic primitive equations	Non-hydrostatic equations
Physics	Parametrized subgrid precipitation	Fully explicit precipitation
Lateral boundary conditions	None	From ARPEGE forecasts

Table 2. Specific features of data assimilation and EDA in ARPEGE and AROME.

	ARPEGE	AROME
Assimilation scheme	4D-Var	3D-Var
Assimilation cycle	6 h	3 h
Assimilated observations	Conventional + satellite	Conventional + satellite + radar
Auto-covariance modelling (in **B**)	Flow-dependent variances	Homogeneous climatological variances
Cross-covariance modelling (in **B**)	Partly flow-dependent balances	Static homogeneous balances
	No balance for specific humidity	Balance for specific humidity
Model error representation in EDA	Inflation of forecast perturbations	None

90 member global ARPEGE ensemble. Specificities of AROME and ARPEGE are summarized in Tables 1 and 2. The AROME ensemble uses the AROME-France model, which is a limited-area model based on a 2.5 km resolution. Thanks to this high resolution, non-hydrostatic dynamics and a comprehensive microphysical parametrization can be used. This allows the life cycle of clouds and the underlying diabatic processes to be represented explicitly. The AROME-France model uses a 3D-Var analysis scheme every 3 h and the same observation types as in ARPEGE are assimilated, with two exceptions:

- the SEVIRI radiances are used at higher resolution and not only for clear sky over sea but also above low clouds (Montmerle *et al.*, 2007); and
- the radar data (Doppler winds and reflectivities) from the French ARAMIS network are also assimilated (Montmerle and Faccani, 2009; Caumont *et al.*, 2010).

Observation perturbations, which are constructed as random draws of the specified observation-error covariances, are added to real observations in order to simulate observation errors. No model perturbations have been included in the AROME ensemble experiment (i.e. a perfect model assumption is used), except that lateral boundary conditions are perturbed through the coupling to the AEARP ensemble. This AEARP ensemble is a global ensemble data assimilation system, which is designed to simulate the error evolution of the global ARPEGE 4D-Var deterministic system (Berre *et al.*, 2006; Berre and Desroziers, 2010). Its current operational version corresponds to a six-member ensemble of perturbed 4D-Var data assimilation cycles (updated every 6 h). The AEARP ensemble size has been increased to 90 members for the experiments. The AEARP model truncation is $T399$, which corresponds approximately to a 50 km horizontal resolution. Observation perturbations are added to represent observation errors and forecast perturbations are inflated every 6 h (without using any stochastic physics), in order to simulate model error contributions (Raynaud *et al.*, 2012). The AROME ensemble has been started from the deterministic AROME-France background valid on 3 November 2011 at 0600 UTC. A 12 h maturation period has been run, so that background-error covariances have been examined for four successive 3 h cycles starting on 3 November 2011 at 1800 UTC.

3.2. Diagnosis of background-error covariances

The chosen experimental period is characterized by strong convection, as illustrated in Figure 1: a large and intense trough, associated with a low located over the North East Atlantic and a strong jet stream, was advecting moist unstable air from the Mediterranean Sea over Southern France. As can be seen in Figure 2, this leads to a marked contrast between large values of background specific humidity over the Mediterranean Sea, small values over Nothern Spain and Germany and intermediate values over France. When reaching the highlands of the Cévennes region, the Mediterranean unstable air mass generates heavy precipitation, as displayed in Figure 3. A large part of the domain covered by AROME was also subject to organized thunderstorms, especially over France along a north/south axis. Our goal here is thus to examine the connection between background-error covariances and the weather situation, to evaluate sampling noise effects and to compare AEARO and AEARP estimates. In particular, sampling noise aspects have been studied for AEARO by comparing independent 84 member estimates with six-member estimates. Similarly, six-member AEARP estimates have been diagnosed, since this corresponds to the current ensemble size of the operational version of AEARP. These different ensemble configurations are summarized in Table 3. This table of configurations also includes the case in which ensemble-based variances are spatially filtered. The filter applied on the variances of the six-member AEARO and six-member AEARP configurations is a Wiener filter similar to the one used in the operational AEARP version, from Raynaud *et al.* (2009). This objective spectral filter is homogeneous over the domain and is based on an estimation of the average autocovariance functions of

- the ensemble estimate $\widetilde{B}_{ii}$, via the Wiener–Khinchin theorem, and
- the sampling noise $\widetilde{B}_{ii} - \widetilde{B}^*$, via the Wishart theory.

The assumptions and behaviour of this kind of filter will be detailed in a future article.

As explained in the previous subsection, AEARO and AEARP have been designed in order to simulate the error evolution in two different data assimilation systems, namely the regional high-resolution AROME 3D-Var and the global large-scale ARPEGE 4D-Var, respectively. Due to this difference of design, the comparison between AEARO and AEARP ensemble estimates has to be taken with caution. In the context of the present article, a comparison will be made in order to document AEARO features that are either in common with AEARP or specific to AEARO, due for instance to resolution and data assimilation differences. Background-error variances and correlation diagnostics were computed at each level of the AROME grid for several model variables, such as specific humidity, temperature and wind (in terms of zonal/meridional wind and also vorticity/divergence). In the context of a comparison with AEARO estimates, global AEARP
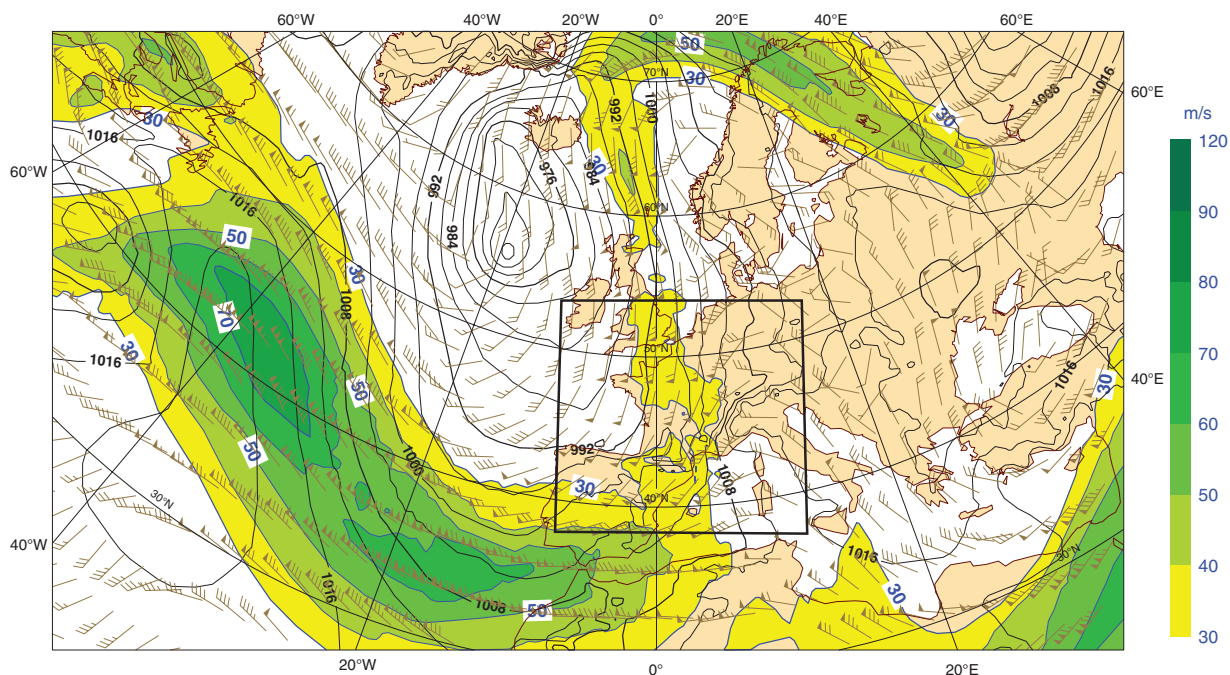
Figure 1. ARPEGE analysis on 3 November 2011 at 1800 UTC. Sea-surface pressure (solid black line, unit: hPa) and wind speed (colour scale, unit: m s^{-1}) at 200 hPa. The AROME domain is indicated.

variance fields were interpolated horizontally and vertically on to the AROME grid. Moreover, when characterizing sampling noise of the AROME six-member ensemble, unbalanced components of humidity and temperature (as defined e.g. in Derber and Bouttier (1999) and Berre (2000), i.e. differences between full variables and their balanced components) were also computed, since they are used in the $\overline{\mathbf{B}}$ model currently used in AROME.

3.3. Evaluation of background-error diagnostics

The 84 member AROME ensemble estimates will be taken as references with respect to the six-member AROME ensemble estimates and denoted with a 'ref' superscript. In this 84 member ensemble, sampling noise is obviously also present, which is not completely satisfying for a reference. Nevertheless, the Wishart theory states that the noise standard deviation of the 84 member estimation is $\sqrt{(84-1)/(6-1)} \simeq 4$ times smaller than the noise standard deviation of the the six-member estimation.

In order to compare estimates associated with different ensembles, the following diagnostic quantities will be examined for a given diagnostic field $\widetilde{\mathbf{p}}$ (corresponding e.g. to a background-error variance field, associated with a set of n grid-point values):

- the horizontal average of $\widetilde{\mathbf{p}}$:

$$\mu(\widetilde{\mathbf{p}}) = \frac{1}{n} \sum_{i=1}^{n} \widetilde{p}_i; \qquad (15)$$

and
- the spatial correlation with respect to AEARO-84 estimates,

$$\text{cor}(\widetilde{\mathbf{p}}, \widetilde{\mathbf{p}}^{\text{ref}}) = \frac{\sum_{i=1}^{n} \left(\widetilde{p}_i - \mu(\widetilde{\mathbf{p}}) \right) \left(\widetilde{p}_i^{\text{ref}} - \mu(\widetilde{\mathbf{p}}^{\text{ref}}) \right)}{\sigma(\widetilde{\mathbf{p}}) \sigma(\widetilde{\mathbf{p}}^{\text{ref}})}, \quad (16)$$

where $\sigma(\widetilde{\mathbf{p}})$ is the spatial spread of the field:

$$\sigma(\widetilde{\mathbf{p}}) = \sqrt{\frac{1}{n-1} \sum_{i=1}^{n} \left(\widetilde{p}_i - \mu(\widetilde{\mathbf{p}}) \right)^2}. \qquad (17)$$

In order to characterize sampling noise in AEARO-06 variances and effects of their filtering, the spatial root-mean-square error

(RMSE) with respect to the reference will also be used:

$$\text{RMSE}(\widetilde{\mathbf{p}}, \widetilde{\mathbf{p}}^{\text{ref}}) = \sqrt{\frac{1}{n} \sum_{i=1}^{n} (\widetilde{p}_i - \widetilde{p}_i^{\text{ref}})^2}. \qquad (18)$$

4. Experimental diagnosis of background-error variances

4.1. Examples of flow-dependent features

Examples of flow-dependent error variance estimates are shown in Figure 4, which corresponds to the specific humidity error at level 50 (near 950 hPa). Since humidity at low levels plays an important role in triggering and maintaining the convective activity, error variances of this parameter are particularly interesting to examine. As can be seen in the corresponding top left panel (AEARO-84 estimate), there is a relatively wide area of large variances over the northwest Mediterranean Sea. This contrasts with relatively small values over land in general, although intermediate values (corresponding to local maxima) are visible over southwest France and partly along the main frontal rain band that crosses France.

The large variances over the Mediterranean Sea are related to wide areas with a high amount of water vapour in the associated warm maritime air mass, as can be seen in the background field q_b of specific humidity (Figure 2). Phase and amplitude errors in specific humidity in this moist area thus imply relatively large error variances. This can be compared with the smaller error variances in relatively drier areas (as shown by the q_b map), e.g. over France and even more markedly in North Spain and near Alpine areas. The intermediate values over southwest France are likely to reflect uncertainties when predicting the convergence zone of low- to mid-level humidity in the vicinity of convective areas.

The AEARO-84 estimate can be compared with the AEARP-84 estimate (bottom left panel). On the one hand, the large-scale contrast between large variances over the Mediterranean Sea and smaller values over land is also visible in the AEARP-84 field. This is consistent with the high amount of water vapour in the maritime air mass, which is also represented in ARPEGE. On the other hand, the local variance maxima over southwest France are not much visible in AEARP-84. This is likely to be related to resolution differences in particular, which imply that
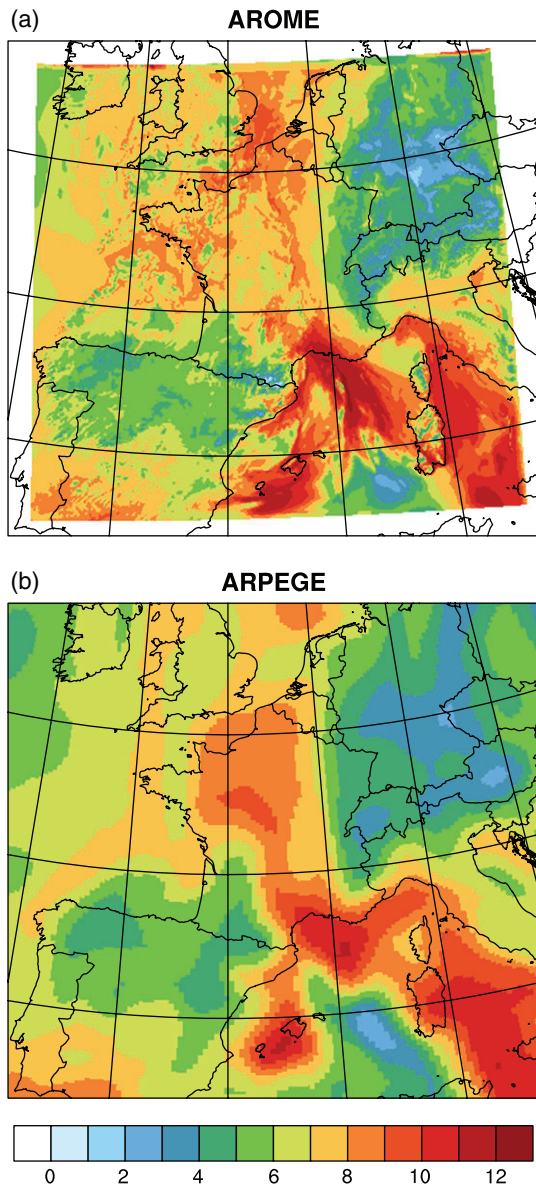
(a) AROME

(b) ARPEGE

Figure 2. Specific humidity 3 h forecast at level 50 ($\sim$ 945 hPa), from the 3 November 2011, 1800 UTC analysis (unit: g kg^{-1}). (a) First member of the AROME ensemble. (b) First member of the ARPEGE ensemble.

Figure 3. Radar reflectivity from the French radar network ARAMIS on 3 November 2011 at 2100 UTC (unit: dBZ).

Table 3. Experimental configurations.

System	Resolution	Filtering	Ensemble size
AEARO	2.5 km	No	84
			6
		Yes	6
AEARP	T399	No	84
			6
	T224	Yes	6

the convective activity driven by orography is less in AEARP, due to its lower resolution. Finally, large variances are locally amplified for AEARO near the southern and eastern boundaries, probably due to coupling artefacts.

4.2. Sampling noise aspects

The top middle panel (AEARO-06) in Figure 4 can be compared with the top left panel (AEARO-84), in order to examine sampling noise associated with the AROME six-member estimate. On the one hand, large-scale structures of AEARO-84 are clearly visible in the AEARO-06 estimate, such as the wide Mediterranean area affected by large error variances. On the other hand, there are many small-scale features in AEARO-06 that do not coincide with AEARO-84, for instance regarding the amplitude, location and extension of the local variance maxima around northwest France. This suggests that sampling noise is on a relatively small scale compared with the signal of interest.

This is supported by Figure 5, in which the respective energy spectra of AEARO-06 and AEARO-84 are plotted. Differences between these two spectra can be interpreted as corresponding to the sampling noise amplitude of the six-member estimate relative to the 84 member estimate. As expected from the previous
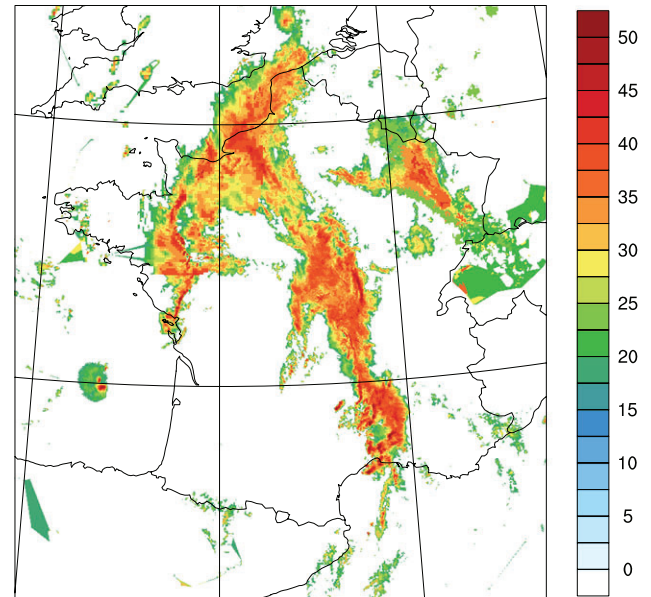
discussion about Figure 4, it appears that the noise-to-signal ratio is relatively small at large scales and relatively large at small scales.

This suggests that the application of an objective spatial filter should be beneficial in order to reduce sampling errors. The corresponding effect of such a filter on the error variance map is illustrated in the top right panel of Figure 4. As expected, the large-scale robust structures are preserved, while the small-scale noisy details tend to be filtered out. As a consequence, compared with the raw AEARO-06 variance field, the filtered AEARO-06 field is much closer to AEARO-84, as can be seen e.g. from the lesser amount of spurious local spots than in the raw AEARO-06 variance field. Sampling noise features can also be examined for AEARP, by comparing the AEARP-06 estimate (bottom middle panel of Figure 4) with the AEARP-84 estimate (bottom left panel). On the one hand, the large-scale contrast in AEARP-84 between the Mediterranean Sea and the continental area is also visible in AEARP-06. On the other hand, the spatial structure of the Mediterranean variance field looks more patchy in AEARP-06 than in AEARP-84. This is an analogous indication that, in the AEARP context, the sampling noise is smaller scale than the signal of interest in AEARP-84. As expected, application of an objective spatial filter (bottom right panel of Figure 4) allows the AEARP-06 patchiness to be reduced.

It may also be noticed that sampling noise is likely to be larger scale in AEARP than in AEARO. This is supported by the comparison between respective energy spectra of the AEARP-06 and AEARP-84 variance maps in Figure 5, which indicates that sampling noise in AEARP-06 is typically significant below 300 km. This is consistent with Eq. (11) and with resolution differences between AEARP and AEARO: since background-error correlations are larger scale in AEARP than in AEARO (e.g. Brousseau *et al.*, 2011 in a related context), Eq. (11) indicates that AEARP sampling noise is also expected to be larger scale than
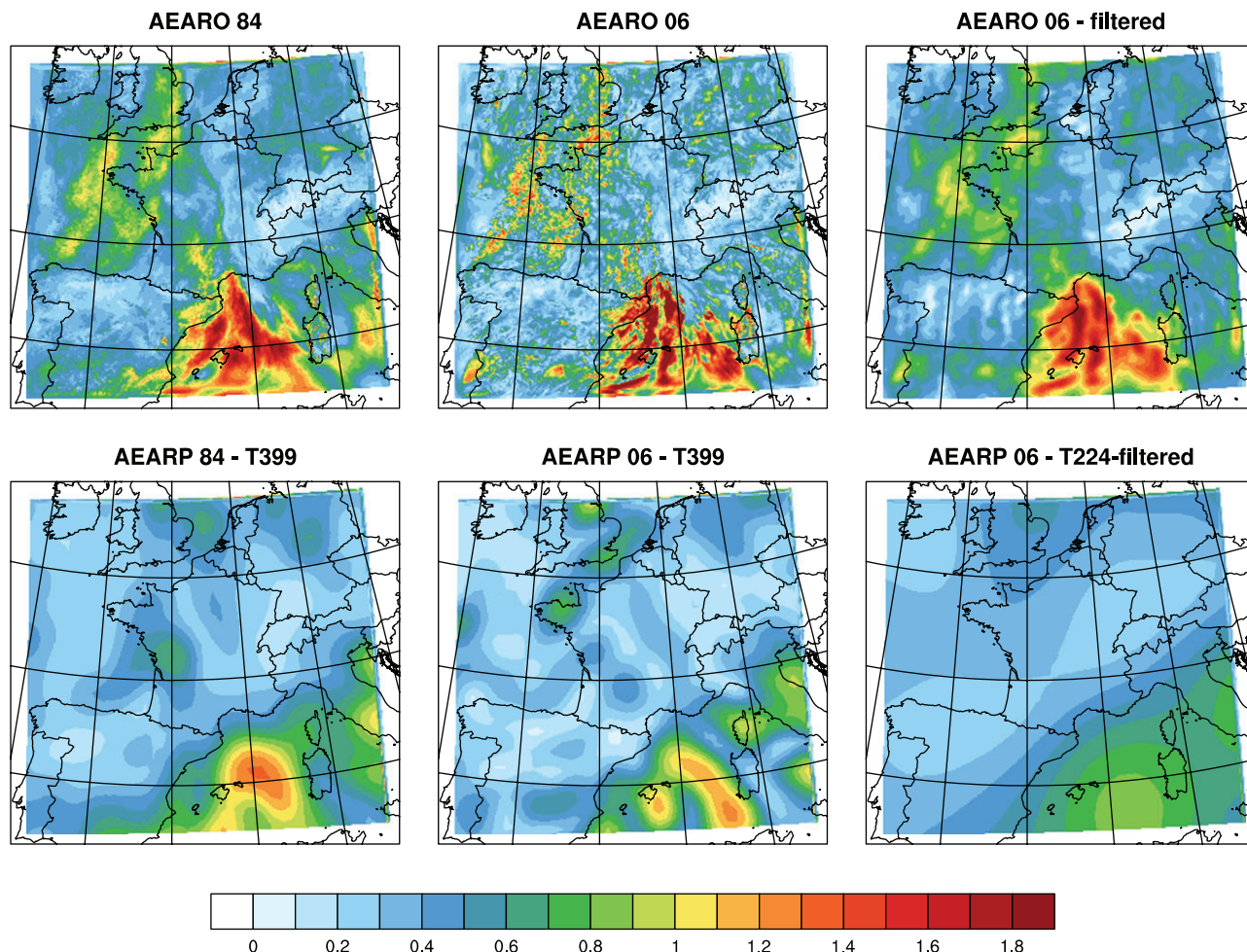
Figure 4. Background-error standard deviations of specific humidity at level 50 (~ 945 hPa) for the six experimental configurations (cf. Table 3). Unit: $g^2 kg^{-2}$.
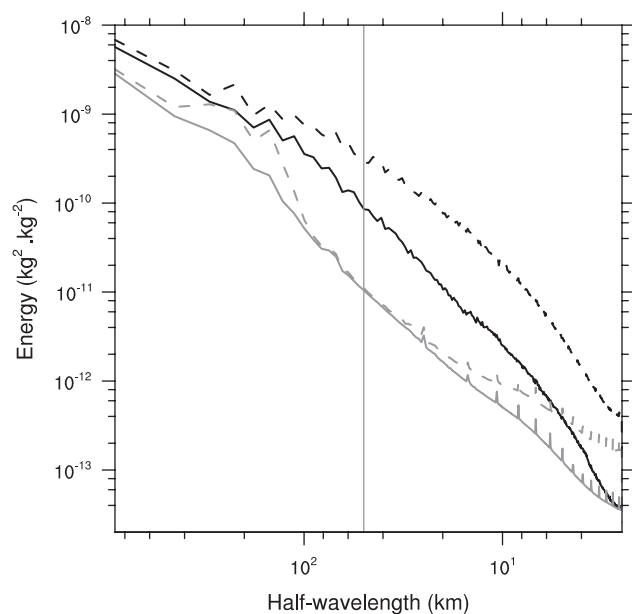

Figure 5. Vertically averaged energy spectra of background-error variances for specific humidity. AEARO and AEARP systems are represented (black and grey lines, respectively) for 84 and six-member ensembles (solid and dashed lines, respectively). The vertical grey line indicates the 50 km half-wavelength, below which the variances are interpolated for the AEARP system.

4.3. Square root of horizontally averaged error variances

The vertical profiles of square roots of horizontally averaged variances of background error are displayed in Figure 6. As expected, the AEARO average values on this date (3 November 2011) are larger than the climatological values (not shown) that are used in the specification of $\overline{\mathbf{B}}$ in the operational version of the AROME-France 3D-Var; these have been computed during a spring period that was partly anticyclonic (Brousseau *et al.*, 2011). This is related to the intense weather phenomena occurring on the chosen date, which are associated with relatively large uncertainties. For specific humidity variances, this also reflects the influence of the larger amount of water vapour on this date, compared with the relatively cold and dry period used in the climatological estimates. A preliminary comparison with observation-based estimates (Desroziers *et al.*, 2005) of AROME background-error variances has also been performed (not shown). As expected from the perfect model assumption, the results indicate that the current AEARO background-error variances are underestimated by approximately a factor of 2, which is consistent with previous studies in global models (e.g. Houtekamer *et al.*, 2009; Raynaud *et al.*, 2012). The comparison between AROME and ARPEGE profiles indicates that horizontally averaged variances of AEARO are larger than in AEARP. This is also consistent with previous studies, which have examined the effect of model resolution on average background-error variances (e.g. Stefanescu *et al.*, 2006; Brousseau *et al.*, 2011). The increase of variance in AEARO can thus be interpreted as corresponding to the contribution of small-scale structures that are represented specifically in AROME (i.e. not in ARPEGE), which corresponds to scales smaller than 50 km. In accordance with previous related studies (see e.g. figure 3 in Stefanescu *et al.* (2006) and figure 2 in Brousseau *et al.* (2011)), this increase of variance is much
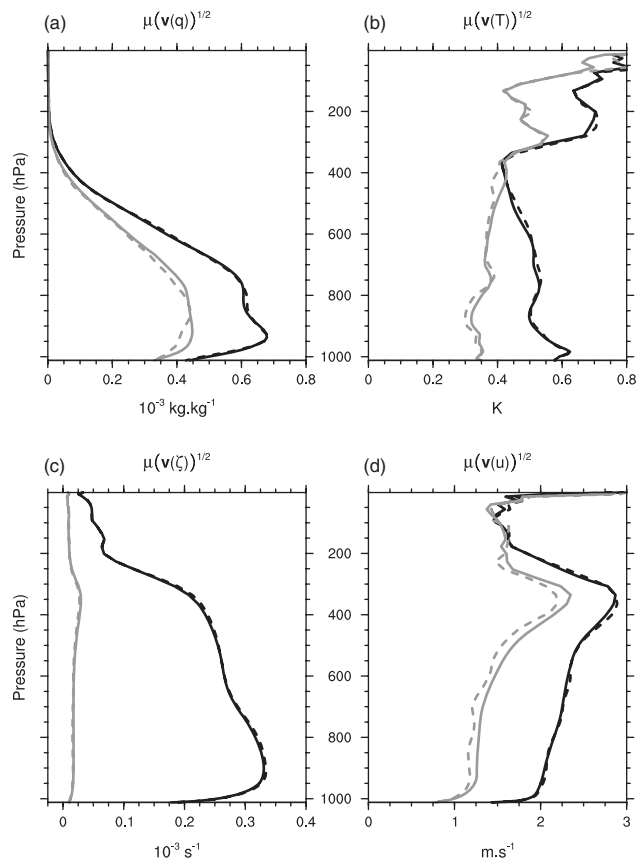
in AEARO. Note also that scales below 50 km are determined by the interpolation of the AEARP variance fields on to the AROME grid. While their amplitudes are relatively small, spectral features below 50 km are thus not really meaningful, in the sense that they are dominated by interpolation errors.

Figure 6. Square root of the spatial average of background-error variances, for AEARO-84 (solid black), AEARO-06 (dashed black), AEARP-84 (solid grey) and AEARP-06 (dashed grey). The panels show (a) specific humidity (q), (b) temperature (T), (c) vorticity (ζ) and (d) zonal wind (u).

Figure 7. Spatial correlation of background-error variances with respect to AEARO-84, for AEARO-06 (dashed black), AEARP-84 (solid grey) and AEARP-06 (dashed grey). The panels show (a) specific humidity (q), (b) temperature (T), (c) vorticity (ζ) and (d) zonal wind (u).

more pronounced for vorticity than for wind, temperature and humidity. This corresponds to the fact that vorticity is a spatial derivative of zonal/meridional wind, which is thus much more sensitive to model resolution than e.g. zonal/meridional wind and temperature.

4.4. Spatial correlation between error variance maps

The vertical profiles of average correlations between AEARO-84 variance estimates and other estimates are shown in Figure 7. The correlation values between AEARO-84 and raw AEARO-06 estimates typically vary between 0.6 and 0.8, which indicates that raw AEARO-06 variances capture a relatively large part of the signal present in AEARO-84 estimates. These correlation values are increased further by approximately 10% (not shown) after applying a spatial filter to the raw AEARO-06 variance field, thanks to the attenuation of small-scale noisy structures. The correlations between AEARP-84 and AEARO-84 variance maps are also plotted in Figure 7. These are interesting to look at, in order to evaluate the respective effects of common flow-dependent features and AROME-specific aspects. The largest values are found for specific humidity, with correlations typically in the range [0.4:0.7]. This is likely to correspond to the large-scale Mediterranean area affected by large humidity error variances, as represented in both AEARP and AEARO. On the other hand, AEARP-84 correlations are smaller than e.g. AEARO-06 correlations, as expected from the specific small-scale structures represented in AEARO. This effect is more pronounced for temperature, while the wind case is intermediate. This may be related to specific small-scale structures of temperature perturbations in AEARO, related to convection for instance. The increase of values above 250 hPa can be explained by the spectral nudging of AROME forecast fields toward ARPEGE values, which increases linearly with height in the stratosphere. It can also be noted that correlations between AEARP and AEARO variance fields are much smaller for vorticity than for wind.
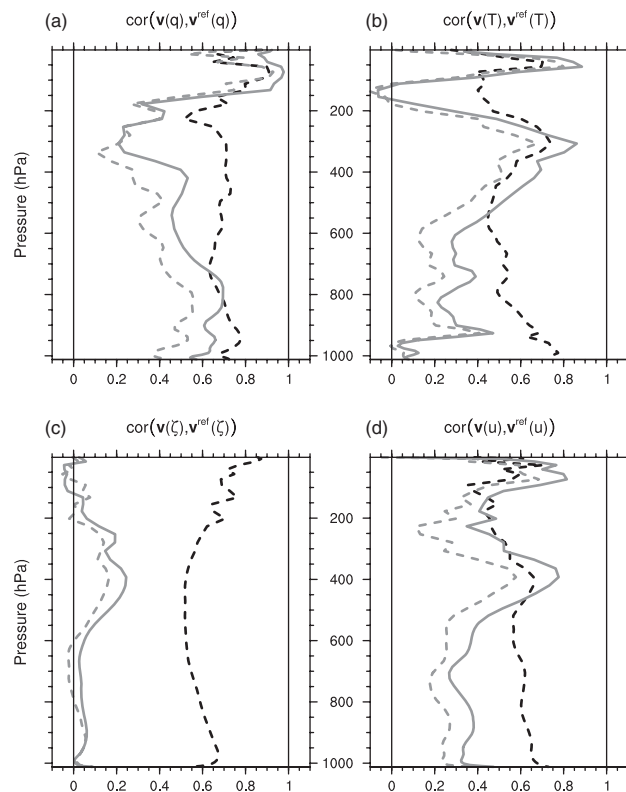
This reflects the fact that vorticity is very dependent on the model resolution, as discussed before. Finally and as expected from reduced sampling noise effects, it can also be seen that correlations are larger by approximately 10% for AEARP-84 than for AEARP-06.

4.5. Spatial RMSE of raw/filtered AEARO variance maps

Another way to examine the effects of sampling noise and of their spatial filtering is to compute the root-mean-square error RMSE($\widetilde{\mathbf{v}}, \widetilde{\mathbf{v}}^{\text{ref}}$) of background-error variances of AEARO-06 configurations with respect to the reference (Figure 8). Since here we focus only on AROME variables, results for unbalanced temperature (T_u), specific humidity (q_u) and divergence (η_u) are shown (vorticity being treated in a univariate way (Berre, 2000)).

The RMSE of raw AEARO-06 variances is interesting to compare with the RMSE of static homogeneous variances (denoted by OPER) used in the current operational AROME version. Because of the large amount of sampling noise in raw AEARO-06 variances, it can be seen that their RMSE is larger than the OPER RMSE for temperature and vorticity, although the raw AEARO-06 RMSE is smaller for low-level humidity.

These AEARO-06 RMSE values are reduced significantly when applying the spatial filter, as can be seen for specific humidity in particular. This leads to smaller RMSE than in OPER for humidity, temperature and low-level vorticity, while RMSE values remain slightly larger for mid-level vorticity.

These improvements associated with the spatial filter result not only from increased correlation values with AEARO-84 fields but also from a beneficial reduction of the exaggerated spatial spread $\sigma_\mu(\widetilde{\mathbf{v}})$ of the raw AEARO-06 variance fields. These results are encouraging and let us believe that more efficient filters could increase these improvements further.
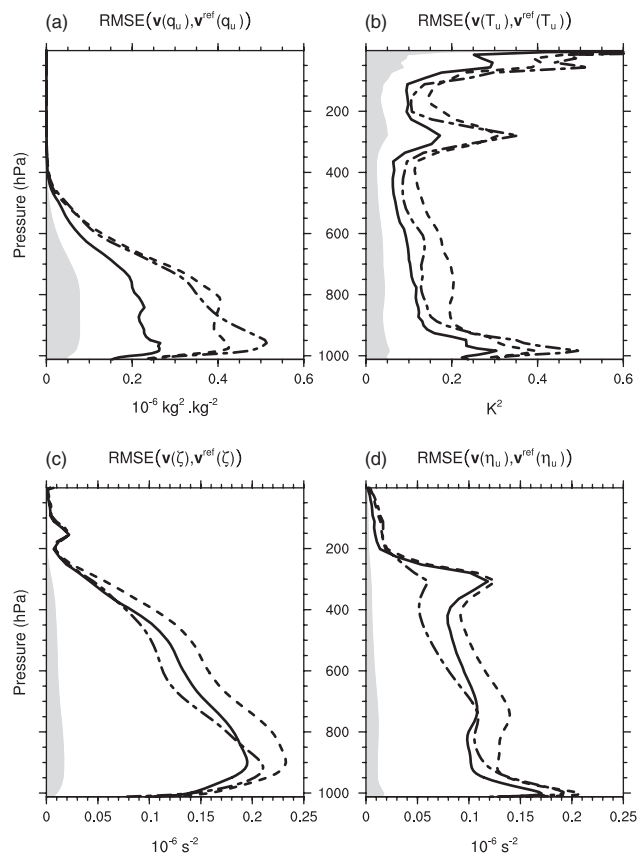
Figure 8. RMSE of background-error variances with respect to the reference AEARO-84, for the operational climatology (dash−dotted black), AEARO-06 (dashed black) and AEARO-06 filtered (solid black). The panels show (a) unbalanced specific humidity (q_u), (b) unbalanced temperature (T_u), (c) vorticity (ζ) and (d) unbalanced divergence (η_u). The shaded area estimates the standard deviation of the noise of the reference due to subsampling.

5. Experimental diagnosis of background error LCH tensors

5.1. Estimation issues

In the continuous case, Belo Pereira and Berre (2006) showed that the components of the tensor H can be expressed from an ensemble of perturbations δ by

$$H_{\alpha\beta}^{\mathrm{BPB}} = \left(\mathrm{cov}\left(\frac{\partial \delta}{\partial x_\alpha}, \frac{\partial \delta}{\partial x_\beta} \right) - \frac{\partial \sigma(\delta)}{\partial x_\alpha}\frac{\partial \sigma(\delta)}{\partial x_\beta} \right) \sigma(\delta)^{-2}, \quad (19)$$

where x_α and x_β are spatial basis coordinates and the BPB superscript refers to Belo Pereira and Berre (2006). While this formula can be applied to estimate correlation length-scales, its application for anisotropy diagnostics is potentially more difficult, in the sense that the positive-definiteness of estimated tensors is not guaranteed when using this formula. This is likely to arise more frequently when standard-deviation gradients are spuriously large due to sampling noise, which is likely to make the negative term $-(\partial \sigma(\delta)/\partial x_\alpha)(\partial \sigma(\delta)/\partial x_\beta)$ excessively large.

This issue is illustrated in Figure 9, which corresponds to the proportion of cases where H^{BPB} is non-positive-definite, for large and small ensembles. While the positive-definiteness appears to be ensured for 90 member estimates for all variables except for vorticity, the proportion of non-positive-definite cases is significant for six-member estimates and it is particularly large for vorticity. There are several possible ways to treat this issue. One possible approach (used in Raynaud and Pannekoucke, 2012) is to consider that local variances are nearly homogeneous locally, which allows the standard deviation derivative to be cancelled. Another possible method could be to use spatially filtered variances, in order to employ less noisy and thus more realistic amplitudes for the standard deviation derivative term. In
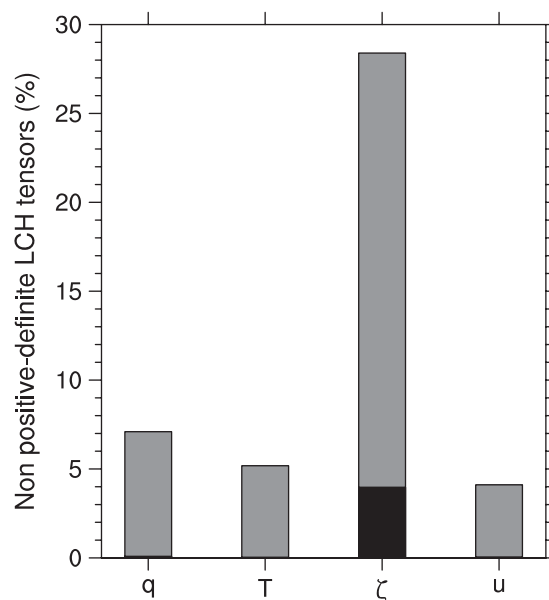

Figure 9. Proportion of cases where LCH tensors estimated with the Belo Pereira and Berre (2006) formula are not positive-definite, for the AEARO ensemble with six-member (grey) and 84 member (black) subsamples, considering the following fields: specific humidity (q), temperature (T), vorticity (ζ) and zonal wind (u).
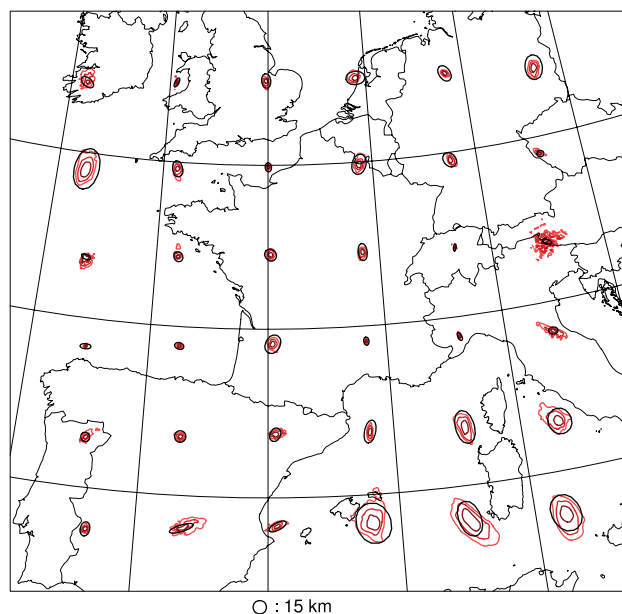

○ : 15 km

Figure 10. Background-error correlations of specific humidity at level 50 ($\sim$ 945 hPa), for the AEARO configuration with a large ensemble (84 members). Black thick ellipses represent the LCH tensor (see text) adjusted with a constant scaling factor and thin lines the correlation isocontours 0.7, 0.8 and 0.9.

the current article, we have chosen to use a third method, following Michel (2012), who found recently a compact formulation of H as covariances of normalized perturbation derivatives:

$$H_{\alpha\beta}^{\mathrm{M}} = \mathrm{cov}\left(\frac{\partial \left(\delta/\sigma(\delta) \right)}{\partial x_\alpha}, \frac{\partial \left(\delta/\sigma(\delta) \right)}{\partial x_\beta} \right), \quad (20)$$

where the M superscript refers to Michel (2012). This formulation can be seen as a particular case of Eq. (19), applied to the normalized perturbation $\delta' = \delta/\sigma(\delta)$. It is straightforward to show that the H^{M} formulation ensures that the estimated tensor is positive-definite, since it is computed as a typical covariance matrix of N vectors $\nabla\left(\delta_k/\sigma(\delta)\right)$. The results shown thereafter are thus obtained from this formulation.
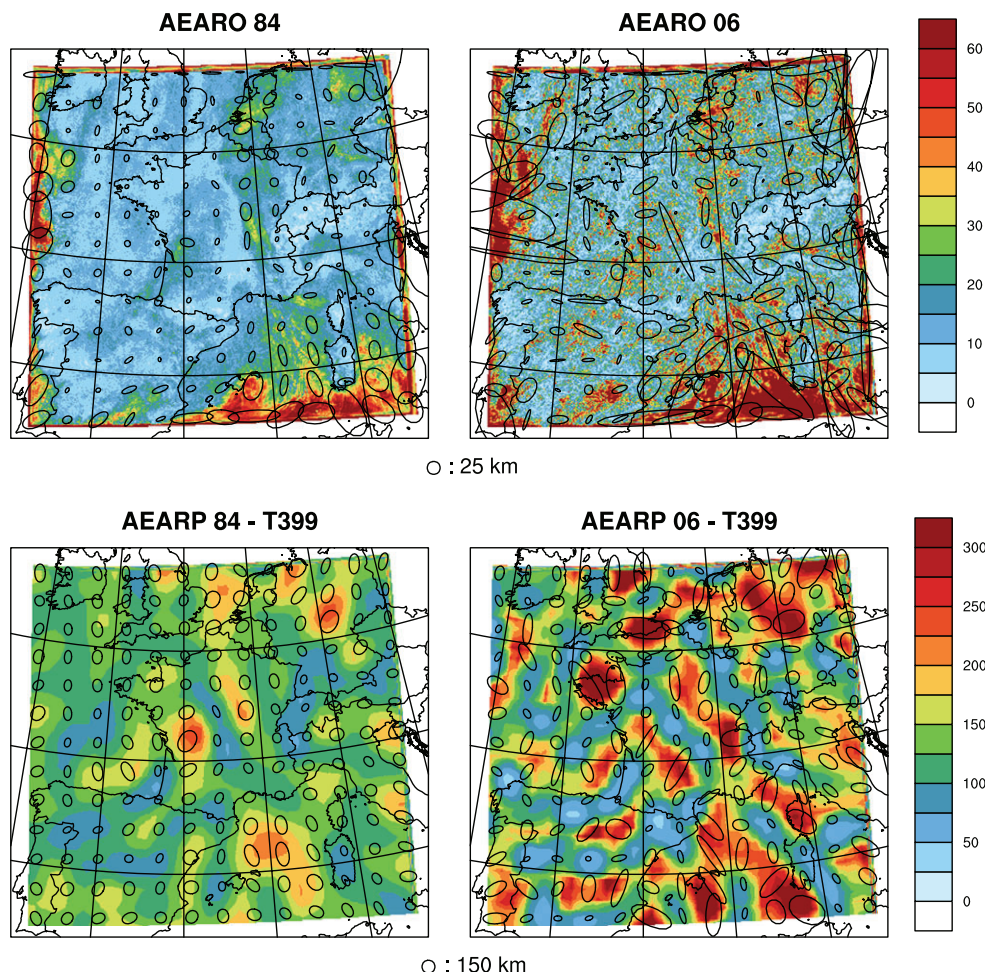
Figure 11. Background-error LCH tensor of specific humidity at level 50 (∼ 945 hPa), for AEARO and AEARP configurations with large and small ensembles. Ellipses represent the LCH tensor (see text) adjusted with a constant scaling factor and total length-scales are represented using a colour scale. Unit: km.

5.2. LCH tensor relevance

The ellipse representing a LCH tensor can be interpreted as a first-order approximation of the correlation function shape around the origin. Indeed, Figure 10 shows a close connection between the ellipse shape and isocontours between 0.7 and 0.9, tensors and correlations being estimated with 84 members here. However, this property does not hold in regions of rapidly varying topography (such as the Alps in Figure 10), where the horizontal correlation function at a given hybrid level seems very complicated and is not well described by a LCH tensor. As expected from its definition, the LCH tensor does not represent anisotropies which affect long-distance correlations either (not shown). In the current article, the LCH tensor will thus be used to diagnose heterogeneities and anisotropies that affect short-distance correlations.

5.3. Examples of flow-dependent correlation features

The LCH tensor representation and the total length-scales are shown in Figure 11, for the specific humidity error at level 50 (near 950 hPa), i.e. the same variable and level as in Figure 4. The top left panel of this figure corresponds to the AEARO-84 estimates. It can be seen that length-scales tend to be relatively large over the Mediterranean Sea, compared for instance with small values over mountainous areas, such as the Pyrenees, the Alps and Corsica (in accordance with e.g. figure 10 of Deckmyn and Berre (2005)). This is likely to reflect the influence of the large-scale weather situation in the Mediterranean area, with correlation functions that tend to be elongated in the direction of the meridional flow. Relatively large values of length-scale are also visible near the lateral boundaries, as expected from the influence of the large-scale coupling model. It can be seen

that the associated large-scale perturbations tend to be advected towards the inner area of the AROME model near the western and southern boundaries, while this is much less visible in the outflow eastern and northern boundaries.

Over France for instance, one may also notice a tendency to have relatively small (respectively large) length-scales in areas affected by large (respectively small) variances, such as over the northwest and central–south parts of France. This is likely to reflect the influence of small-scale convective structures in these areas, as supported e.g. by Figure 3 and the results in Montmerle and Berre (2010).

The AEARP-84 length-scale diagnostics are shown in the bottom left panel of Figure 11. As expected, correlation length-scales are much larger in AEARP than in AEARO. As discussed in e.g. Daley (1991) and Berre (2000), this is related to the fact that the length-scale L (which is sometimes called the microscale) is very sensitive to the small-scale part of the spectrum, which depends a lot on model resolution (see e.g. figure 3 of Brousseau *et al.* (2011)). For this reason, such length-scales are difficult to compare between AEARO and AEARP. Despite this, areas with relatively large length-scale values can be noticed partly for both 84 member configurations, over the Mediterranean Sea and on both sides of a north/south oriented band of small values that crosses France. Structures linked to the large-scale circulation are thus partly visible in the global and regional models, but AROME generates smaller scale structures (associated with small length-scales), in accordance with its specific resolution and data assimilation.

5.4. Sampling noise aspects

The corresponding map of correlation diagnostics for AEARO-06 is shown in the top right panel of Figure 11. On the one hand, it
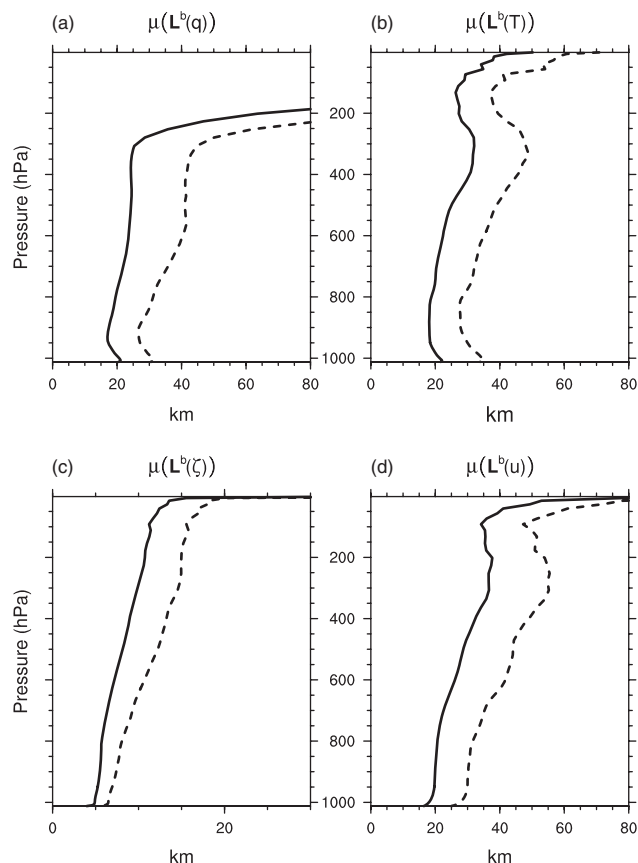
Figure 12. Vertical profiles of horizontally averaged length-scales of background error, for AEARO-84 (solid black) and AEARO-06 (dotted black). The panels show (a) specific humidity (q), (b) temperature (T), (c) vorticity (ζ) and (d) zonal wind (u).
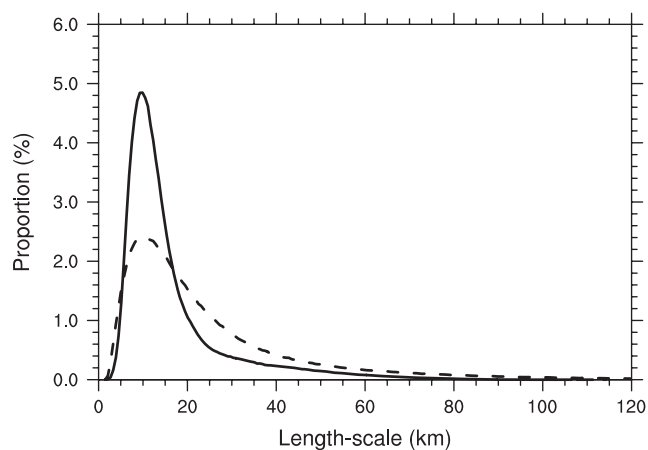

Figure 13. Distributions of specific humidity background-error length-scale at level 50 (~ 945 hPa), for AEARO-84 (solid black) and AEARO-06 (dotted black).

can be seen that there are features that are common with AEARO-84 estimates, such as the large Mediterranean length-scales and the small length-scale values in mountainous areas. On the other hand, it can also be noticed that length-scale maxima in AEARO-06 tend to be exaggerated in amplitude and also tend to be less structured spatially than in AEARO-84, as can be seen from the increased occurrence of spurious local spots.

Vertical profiles of horizontally averaged length-scales are shown in Figure 12. They indicate that AEARO-06 estimates are systematically larger than AEARO-84 length-scales, by approximately 25–50%. This is consistent with the expected positive bias in local length-scales estimates when using a finite-size ensemble, as discussed in Pannekoucke *et al.* (2008). Distributions of background error length-scales are shown in Figure 13 for the specific humidity at level 50. It appears, for

instance, that in AEARO-06 (compared with AEARO-84) the proportion of 10 km values (corresponding to the distribution peak) is underestimated by a factor of 2, while e.g. the proportion of 30 km values is overestimated by a factor of 2, leading to a relatively large positive bias.

These sampling noise effects are even more pronounced with respect to anisotropy estimates (as is visible for both six-member configurations of AEARO and AEARP). This anisotropy is illustrated for some arbitrary locations in Figure 11 by plotting ellipses, the axes and orientation of which are linked to values of the LCH tensor. This illustrates clearly that local anisotropies diagnosed with a six-member configuration tend to be exaggerated compared with a 84 member configuration.

Despite these limitations, spatial correlations $\mathrm{cor}(\widetilde{L}^b, \widetilde{L}^{b\,\mathrm{ref}})$ (not shown) between the total length-scale field estimated from AEARO-06 and the corresponding 84 member reference are almost always larger than 50% for vorticity and 70% for other variables, which is relatively high. These results thus indicate that there is potentially some information on local correlations in AEARO-06, but that appropriate filtering techniques (and eventually more members) are required in order to reduce sampling noise.

6. Conclusions

In order to estimate and diagnose flow-dependent error covariances at the convective scale, a 90 member AROME ensemble data assimilation experiment has been run, coupled to a 90 member ARPEGE large-scale ensemble. This has been carried out through a case study in the frame of HYMEX, which focuses on intense weather events over the Western Mediterranean in particular.

The flow dependence of error covariances has been illustrated for low-level specific humidity, which is characterized e.g. by relatively large error variances over the Mediterranean Sea. This is related to the high amount of water vapour in the associated maritime air mass, as represented in both AROME and ARPEGE ensembles.

Specific features in AROME related to its high resolution are also visible, e.g. larger variances in the southwest part of France than in the ARPEGE ensemble. In accordance with previous related studies, average variances are also larger in AROME than in ARPEGE and correlation length-scales are much smaller in AROME, as expected from resolution differences. These specific features support the strategy to implement a real-time AROME ensemble assimilation system, in order to estimate flow-dependent error covariances that are characteristic of the convective-scale AROME-France model.

Sampling noise features in the variance fields have also been examined, by comparing independent six-member and 84 member estimates, based on the typical small ensemble size planned for a future research experiment. While the six-member ensemble contains relevant information on the flow-dependent covariances, it appears that sampling noise is significant and associated with spurious small-scale structures in the variance fields, for instance. Experiments indicate that this sampling noise can, however, be reduced by applying an objective spatial filter.

A preliminary diagnosis of LCH tensors has also been conducted. Large length-scales are visible over the Mediterranean Sea and also near lateral boundaries. A tendency to have smaller length-scales in regions affected by large variances has been noticed too, which can be associated with small-scale perturbations related to convection. While part of the relevant signal is visible in the six-member ensemble, sampling noise is again found to be significant. This leads to a positive bias in the length-scale estimates and also to spurious small-scale structures in the length-scale field. This latter effect tends to be more pronounced for local anisotropy diagnostics. This issue and the encouraging results of the variance filtering suggest, therefore, that filtering techniques are also likely to be useful for correlation

features. Moreover, the strong heterogeneities and anisotropies observed for convective-scale LCH tensors (e.g. due to coupling fields) lead us to think that a homogeneous and isotropic localization in convective-scale EnKF, hybrid or EnVar systems would be sub-optimal. The clear link between correlation structures and LCH tensors, except in steep topography areas, suggests that LCH tensors could be useful to compute heterogeneous localizations, but this matter is beyond the scope of this article. Future studies will focus on comparisons of different homogeneous and heterogeneous filters to reduce sampling noise effects for forecast-error variances and LCH tensors. The most appropriate techniques will then be exploited to provide robust flow-dependent covariances to the deterministic and ensemble versions of AROME 3D-Var.

Acknowledgements

References

Belo Pereira M, Berre L. 2006. The use of an ensemble approach to study the background error covariances in a global NWP model. *Mon. Weather Rev.* **134**: 2466–2489.

Berre L. 2000. Estimation of synoptic and mesoscale forecast error covariances in a limited-area model. *Mon. Weather Rev.* **128**: 644–667.

Berre L, Desroziers G. 2010. Filtering of background error variances and correlations by local spatial averaging: A review. *Mon. Weather Rev.* **138**: 3693–3720.

Berre L, Stefanescu S, Belo Pereira M. 2006. The representation of the analysis effect in three error simulation techniques. *Tellus A* **58**: 196–209.

Brousseau P, Berre L, Bouttier F, Desroziers G. 2011. Background-error covariances for a convective-scale data-assimilation system: AROME-France 3D-Var. *Q. J. R. Meteorol. Soc.* **137**: 409–422.

Brousseau P, Berre L, Bouttier F, Desroziers G. 2012. Flow-dependent background-error covariances for a convective-scale data assimilation system. *Q. J. R. Meteorol. Soc.* **138**: 310–322.

Buehner M, Houtekamer PL, Charette C, Mitchell HL, He B. 2009a. Intercomparison of variational data assimilation and the ensemble Kalman filter for global deterministic NWP. Part I: Description and single-observation experiments. *Mon. Weather Rev.* **138**: 1550–1566.

Buehner M, Houtekamer PL, Charette C, Mitchell HL, He B. 2009b. Intercomparison of variational data assimilation and the ensemble Kalman filter for global deterministic NWP. Part II: One-month experiments with real observations. *Mon. Weather Rev.* **138**: 1567–1586.

Caron JF, Fillion L. 2010. An examination of background error correlations between mass and rotational wind over precipitation regions. *Mon. Weather Rev.* **138**: 563–578.

Caumont O, Ducrocq V, Wattrelot E, Jaubert G, Pradier-Vabre S. 2010. 1D+3DVar assimilation of radar reflectivity data: A proof of concept. *Tellus A* **62**: 173–187.

Daley R. 1991. *Atmospheric Data Analysis*. Cambridge University Press: Cambridge, UK.

Deckmyn A, Berre L. 2005. A wavelet approach to representing background error covariances in a limited-area model. *Mon. Weather Rev.* **133**: 1279–1294.

Derber J, Bouttier F. 1999. A reformulation of the background error covariance in the ECMWF global data assimilation system. *Tellus A* **51**: 195–221.

Descamps L, Labadie C. 2009. 'PEARP, the Météo-France ensemble prediction system'. In *9th EMS Annual Meeting, 9th European Conference on Applications of Meteorology (ECAM)*, 28 September–2 October 2009. Toulouse, France. http://meetings.copernicus.org/ems2009.

Desroziers G, Berre L, Chapnik B, Poli P. 2005. Diagnosis of observation, background and analysis-error statistics in observation space. *Q. J. R. Meteorol. Soc.* **131**: 3385–3396.

Dykstra R. 1970. Establishing the positive definiteness of the sample covariance matrix. *Ann. Math. Stat.* **41**: 2153–2154.

Evensen G. 1994. Sequential data assimilation with a nonlinear quasi-geostrophic model using Monte Carlo methods to forecast error statistics. *J. Geophys. Res.* **99**: 10143–10162.

Houtekamer PL, Mitchell HL. 2001. A sequential ensemble Kalman filter for atmospheric data assimilation. *Mon. Weather Rev.* **129**: 123–137.

Houtekamer PL, Mitchell HL, Deng X. 2009. Model error representation in an operational ensemble Kalman filter. *Mon. Weather Rev.* **137**: 2126–2143.

Le Dimet FX, Talagrand O. 1986. Variational algorithms for analysis and assimilation of meteorological observations: Theoretical aspects. *Tellus A* **38A**: 97–110.

Liu C, Xiao Q, Wang B. 2008. An ensemble-based four-dimensional variational data assimilation scheme. Part I: Technical formulation and preliminary test. *Mon. Weather Rev.* **136**: 3363–3373.

Liu C, Xiao Q, Wang B. 2009. An ensemble-based four-dimensional variational data assimilation scheme. Part II: Observing system simulation experiments with advanced research WRF (ARW). *Mon. Weather Rev.* **137**: 1687–1704.

Lorenz EN. 1963. Deterministic nonperiodic flow. *J. Atmos. Sci.* **20**: 130–141.

Michel Y. 2012. Estimating deformations of random processes for correlation modelling: Methodology and the one-dimensional case. *Q. J. R. Meteorol. Soc.* **139**: 771–783.

Michel Y, Auligné T. 2010. Inhomogeneous background error modeling and estimation over Antarctica. *Mon. Weather Rev.* **138**: 2229–2252.

Monteiro M, Berre L. 2010. A diagnostic study of time variations of regionally averaged background error covariances. *J. Geophys. Res.* **115**: D23203, doi:10.1029/2010JD014095.

Montmerle T, Berre L. 2010. Diagnosis and formulation of heterogeneous background-error covariances at the mesoscale. *Q. J. R. Meteorol. Soc.* **136**: 1408–1420.

Montmerle T, Faccani C. 2009. Mesoscale assimilation of radial velocities from Doppler radars in a preoperational framework. *Mon. Weather Rev.* **137**: 1939–1953.

Montmerle T, Rabier F, Fischer C. 2007. Relative impact of polar-orbiting and geostationary satellite radiances in the ALADIN/France numerical weather prediction system. *Q. J. R. Meteorol. Soc.* **133**: 655–671.

Muirhead RI. 2005. *Aspects of Multivariate Statistical Theory*. John Wiley & Sons, Inc.: Hoboken, NJ.

Pannekoucke O, Berre L, Desroziers G. 2008. Background-error correlation length-scale estimates and their sampling statistics. *Q. J. R. Meteorol. Soc.* **134**: 497–508.

Raynaud L, Pannekoucke O. 2012. Sampling properties and spatial filtering of ensemble background-error length-scales. *Q. J. R. Meteorol. Soc.* **139**: 784–794.

Raynaud L, Berre L, Desroziers G. 2009. Objective filtering of ensemble-based background-error variances. *Q. J. R. Meteorol. Soc.* **135**: 1177–1199.

Raynaud L, Berre L, Desroziers G. 2012. Accounting for model error in the Météo-France ensemble data assimilation system. *Q. J. R. Meteorol. Soc.* **138**: 249–262.

Seity Y, Brousseau P, Malardel S, Hello G, Bénard P, Bouttier F, Lac C, Masson V. 2011. The AROME-France convective-scale operational model. *Mon. Weather Rev.* **139**: 976–991.

Stefanescu SE, Berre L, Pereira MB. 2006. The evolution of dispersion spectra and the evaluation of model differences in an ensemble estimation of error statistics for a limited-area analysis. *Mon. Weather Rev.* **134**: 3456–3478.

Weaver AT, Mirouze I. 2012. On the diffusion equation and its application to isotropic and anisotropic correlation modelling in variational assimilation. *Q. J. R. Meteorol. Soc.* **139**: 242–260.

Wiener N. 1949. *Extrapolation, Interpolation, and Smoothing of Stationary Time Series, with Engineering Applications*. Technology Press of the Massachusetts Institute of Technology: Cambridge, MA.

Wishart J. 1928. The generalised product moment distribution in samples from a normal multivariate population. *Biometrika* **20A**: 32–52.